Proceedings of ASME Turbo Expo 2003
Power for Land, Sea, and Air
June 16-19, 2003, Atlanta, Georgia, USA

GT2003-38544

FOREIGN OBJECT DAMAGE OF TWO GAS-TURBINE GRADE SILICON NITRIDES IN A THIN DISK CONFIGURATION

Sung R. Choi, J. Michael Pereira, Lesley A. Janosik, and Ramakrishna T. Bhatt
NASA Glenn Research Center, Cleveland, OH 44135

ABSTRACT

Foreign object damage (FOD) behavior of two commercial gas-turbine grade silicon nitrides, AS800 and SN282, was determined at ambient temperature through post-impact strength testing for thin *disks* impacted by steel-ball projectiles with a diameter of 1.59 mm in a velocity range from 115 to 440 m/s. AS800 silicon nitride exhibited a greater FOD resistance than SN282, primarily due to its greater value of fracture toughness (K_{IC}). The critical impact velocity in which the corresponding post-impact strength yielded the lowest value was $V_c \approx 440$ and 300 m/s for AS800 and SN282, respectively. A unique lower-strength regime was typified for both silicon nitrides depending on impact velocity, attributed to significant radial cracking. The damages generated by projectile impact were typically in the forms of ring, radial, and cone cracks with their severity and combination being dependent on impact velocity. Unlike thick (3 mm) flexure bar specimens used in the previous studies, thin (2 mm) disk target specimens exhibited a unique backside radial cracking occurring on the reverse side just beneath the impact sites at and above impact velocity of 160 and 220 m/s for SN282 and AS800, respectively.

INTRODUCTION

Ceramics, because of their brittle nature, are susceptible to localized surface damage and/or cracking when subjected to impact by foreign objects. It is also true that ceramic components may fail structurally even by soft particles when the kinetic energy of impacting objects exceeds certain limits. The latter case has been often found in aerospace engines in which combustion products, metallic particles or small foreign objects cause severe damage to blade/vane components, resulting in serious structural problems. Therefore, foreign object damage (FOD) associated with particle impact needs to be considered when ceramic materials are designed for structural applications. In view of this importance, a considerable amount of work on impact damage of brittle materials by sharp particles as well as by "blunt" particles or by plates has been accumulated both experimentally and analytically [1-10].

In previous studies [11,12] by the authors, FOD behavior of two representative gas-turbine grade silicon nitrides, AS800 and SN282, was determined at ambient temperature using flexure bar test specimens. Rigidly supported ceramic target flexure specimens were impacted at their centers by *steel ball projectiles* with a diameter of 1.59 mm in a velocity range from 220 to 440 m/s. Post-impact strength of the target specimens impacted was determined as a function of impact velocity to accurately evaluate the severity of impact damage. AS800 silicon nitride exhibited a greater FOD resistance than SN282, due to its greater value of fracture toughness (K_{IC}). The key material parameter, K_{IC}, affecting FOD resistance was further evidenced by the FOD response of an additional equiaxed, fine-grained silicon nitride that exhibited the lowest fracture toughness of the three silicon nitrides tested. The damage generated by projectile impact was typically in the forms of well- or ill-developed ring and/or cone cracks with some limited presence of radial cracks.

The current work, as an extension of the previous studies, investigates FOD behavior of AS800 and SN282 silicon nitrides at ambient temperature using a thin *disk* configuration of target specimens. The target disks were impacted at their centers at velocities ranging from 115 to 440 m/s by 1.59-mm-diameter *steel ball projectiles*. Post-impact strength of each disk specimen impacted was determined in ring-on-ring biaxial flexure as a function of impact velocity to evaluate the severity of impact damage. Fractography was performed before and after post impact strength testing to determine impact morphologies and the nature of strength–controlling flaw configurations.

EXPERIMENTAL PROCEDURES

Materials and Test Specimens

Materials used in this work were the same as those used in the previous work, i.e, commercially available silicon nitrides, AS800 (fabricated by Honeywell Ceramic Components, Torrance, CA, '99 gelcast vintage) and SN282 (fabricated by Kyocera, Vancouver, WA, '00 vintage). These two silicon nitrides are currently considered as strong candidate materials for gas-turbine applications in view of their substantially improved elevated-temperature properties. Both materials are toughened silicon nitrides with microstructures tailored into elongated grain structures. The degree of elongation and the size of grains were greater in AS800 than SN282. AS800 silicon nitride has been used at the NASA Glenn Research Center in life prediction programs [13,14]. The billets for each material were machined into disk test specimens measuring 2.0 mm by 45.0 mm, respectively, in thickness and diameter. The final finishing was completed with a #500

This is a preprint or reprint of a paper intended for presentation at a conference. Because changes may be made before formal publication, this is made available with the understanding that it will not be cited or reproduced without the permission of the author.

Table 1. Basic mechanical and physical properties of AS800 and SN282 silicon nitrides and steel-ball projectiles at ambient temperature [12]

Material	Elastic modulus[1] E (GPa)	Poisson's ratio[1] ν	Density[2] ρ (g/cm^3)	Hardness[3] H (GPa)	Fracture Strength[4]			Fracture toughness[5] K_{IC} (MPa√m)
					Mean strength (MPa)	Weibull modulus	Characteristic strength (MPa)	
AS800 Si_3N_4	309	0.27	3.27	13.6±1.4	775(45)$^{\phi}$	21	795	8.1(0.3)
SN282 Si_3N_4	304	0.28	3.32	15.3±0.2	595(64)	11	623	5.5(0.2)
Chrome steel balls (SAE 52100)	200*	0.30*	7.80*	HRC≥60*	-	-	-	-

Notes: 1. By the impulse excitation technique, ASTM C 1259 [15]; 2. By mass/volume method; 3. By Vickers microhardness indentation, ASTM C 1327 [16]; 4. By four-point flexure with 20/40 mm spans with a total of 20 specimens for each material, ASTM C1161 [17]; 5. By single-edge-precracked-beam (SEPB) method, ASTM C 1421 [18]; * From the manufacturer's data, HRC=Hardness in Rockwell C scale; $^{\phi}$ The numbers in the parentheses indicate ±1.0 standard deviations.

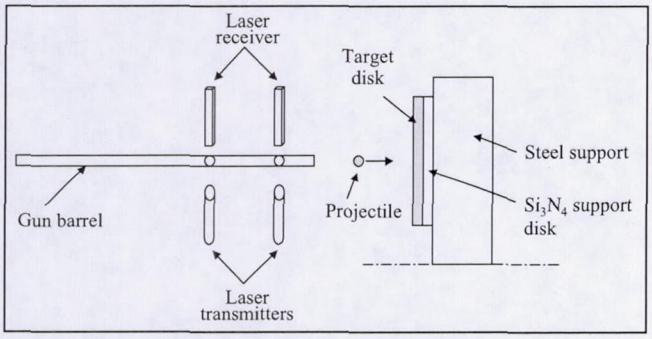

Figure 1. Schematic of impact test arrangements

diamond wheel. The basic mechanical and physical properties of AS800 and SN282 silicon nitrides as well as of the steel-ball projectile material (SAE 52100 chrome steel) are shown in Table 1.

Foreign Object Damage Testing

Foreign object damage (FOD) testing was carried out at ambient temperature using the experimental apparatus shown in Figure 1. A detailed description of the apparatus can be found elsewhere [11,12]. Hardened (HRC≥60) chrome steel-balls with a diameter of 1.59 mm were inserted into a 300mm-long gun barrel with an inner diameter of 1.59 mm. A He-gas cylinder and relief valves were used to pressurize the reservoir to a specific level depending on prescribed impact velocity. Upon reaching a specific level of pressure, a solenoid valve was instantaneously opened accelerating a steel-ball projectile through the gun barrel to impact a target specimen that was rigidly supported on an AS800 disk specimen (2-mm thickness and 45-mm diameter) backed by a metallic specimen holder. Each target specimen was aligned such that the projectile impacted at the center of the test specimen with a normal incidence angle.

For a given pressure, the velocity of each steel projectile was determined using two pairs of laser transmitter and receiver, in which the two transmitters were aimed at the respective receivers through two holes in the gun barrel (see Figure 1). The distance between the two holes was 25 mm, with the front hole located about 70 mm away from the front end of the gun barrel. The time for a projectile to travel between the two holes was measured with a digital storage oscilloscope connected to the two pairs of laser transmitter and receiver. The velocity was then calculated based on the distance-time relationship. A relationship between velocity and pressure was determined in a range of pressure from 0 to 800 psi [12]. It was found that velocity increased with increasing pressure, rising sharply at lower pressure but moderately at higher pressure. The range of impact velocity applied in this work was from 115 to 440 m/s. Typically, 10 test specimens were impacted at each chosen velocity for a given material. Impact morphologies at both impact site and backside of each impacted specimen were examined optically right after impact testing but prior to post-impact strength testing.

Post-Impact Strength Testing

Strength testing for impacted disks was performed in ambient-temperature air to determine the severity of impact damage using a steel ring-on-ring biaxial flexure fixture with 20-mm load-ring and 40-mm support-ring diameters. A series of steel balls were used to eliminate frictional constraint at each of load and support rings, similar to a trust ball bearing assembly. Each impact-tested specimen was coaxially located in the biaxial flexure fixture such that its impact site was placed in tension side. An electromechanical test frame (Model 8562, Instron, Canton, MA) was used in displacement control with an actuator speed of 0.5 mm/min. Slow crack growth occurring during strength testing in air at ambient temperature for some ceramics such as alumina and glass-ceramics was not an issue for the case of most silicon nitrides and silicon carbides. Biaxial flexure strength was calculated based on the analysis by Shetty et al [19]. A fractographic analysis was performed after strength testing to determine failure origin, flaw configuration, and mode of fracture. 'As-received' biaxial strength was also determined for each material with 5 to 8 test specimens using the same test fixture, test frame and test conditions that were utilized for the post-impact strength testing.

RESULTS AND DISCUSSION

Post-impact Strength

The results of two-parameter Weibull distributions of 'as-received' biaxial flexure strength of both AS800 and SN282 silicon nitrides showed that Weibull modulus (m) and characteristic strength (σ_θ) were

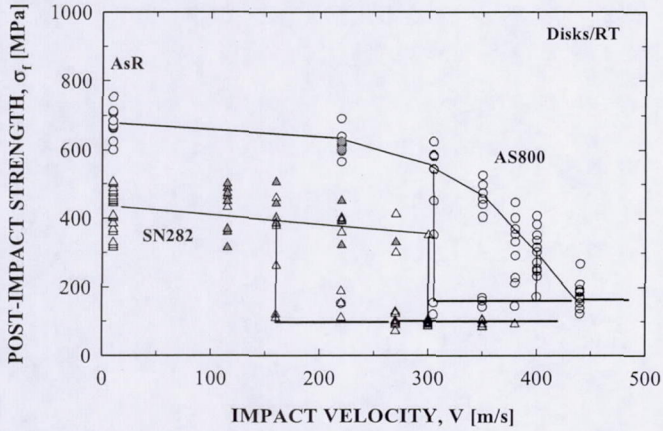

Figure 2. Post-impact biaxial strength as a function of impact velocity, determined for AS800 and SN282 silicon nitrides disks impacted by 1.59-mm-diameter steel ball projectiles at ambient temperature. "AsR" indicates as-received biaxial flexure strength of each material. The open symbols represent the specimens failed from impact sites, while the closed symbols indicate the specimens not failed from impact sites.

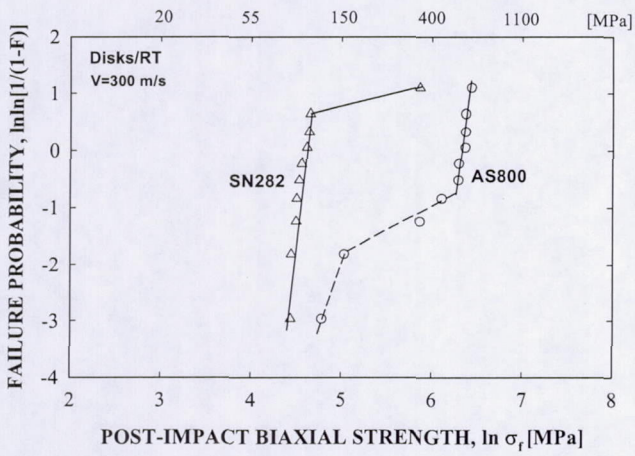

Figure 3. Weibull post-impact biaxial strength distributions of AS800 and SN282 silicon nitrides disks impacted at 300 m/s by 1.59-mm-diameter steel ball projectiles.

m=18 and σ_θ =698 MPa for AS800, and m=8 and σ_θ =451 MPa for SN282, respectively. The mean strength was 678±45MPa for AS800 and 426±60 MPa for SN282. Weibull modulus (m=18, 8 for AS800 and SN282, respectively) in biaxial configuration compares well with that (m=21, 11 for AS800 and SN282, respectively, see Table 1) in uniaxial four-point configuration determined previously [12]. The number of test specimens used in biaxial strength testing was 10 and 21, respectively, for AS800 and SN282.

The results of strength testing for impacted target specimens are shown in Figure 2, where post-impact biaxial flexure strength was plotted as a function of impact velocity for both silicon nitrides. "As-received" biaxial flexure strength of both materials was also included for comparison. Frequently, specimens impacted at low velocities did not fracture from impact sites and were indicated with closed symbols in the figure. For AS800, two specimens out of ten did not fracture from the impact sites at 220 m/s. For SN282, nine, four, two and one specimens (each out of ten) did not fail from the impact sites at 115, 160, 220, and 270 m/s, respectively. Some of these specimens not failed from the impact sites for each material were equivalent in strength to the as-received specimens, and thus used as valid data in estimating the overall as-received biaxial strength of each material.

As seen in the figure, the post-impact strength, in general, decreased with increasing impact velocity. Unlike the post-impact strength of flexure bars [11,12], the post-impact biaxial strength for a given impact velocity (greater than 220 and 160 m/s for AS800 and SN282, respectively) was typified with two distinct regions of strength: higher and lower strength regimes. The strength of the lower regime was around 150 and 100 MPa for AS800 and SN282, respectively. The lower strength regime started at 300 m/s and 160 m/s for AS800 and SN282, respectively. The post-impact strength of each material converged to this lower-regime strength as impact velocity sufficiently increased. This velocity at which a minimum (or the lowest) post-impact strength was retained is called the "critical impact velocity" (V_c) and was found as follows:

$$V_c \approx 440 \text{ m/s for AS800} \qquad (1)$$
$$V_c \approx 300 \text{ m/s for SN282}$$

These critical impact velocities observed for the disks are in good agreement with those observed in flexure bars for AS800 and SN282, V_c=400 and 300 m/s, respectively [11,12]. In the case of flexure bars, the test specimens failed upon impact at the critical impact velocity yielding a *zero* strength due to their small width (4 mm); whereas, in disks the specimens did not fracture upon impact, but instead exhibited radial cracks of significant size while retaining the lower regime strength in strength testing because of the relatively large disk diameter (=45 mm) compared with the size of radial cracks. A fractography section will cover the details regarding impact morphologies, modes of fracture, and other important damage features.

Although not presented here, the two strength regimes were observed more distinctly from Weibull strength plots. The uni-modal strength distribution was characterized in as-received specimens, at lower impact velocities, and at or above critical impact velocities, while the bi- or tri-modality was typified at intermediate impact velocities. A typical example of Weibull plots of both silicon nitrides at an impact velocity of 300 m/s is depicted in Figure 3. Most of the SN282 specimens (9 out of 10) failed at the lower-strength regime with strength around 100 MPa). For AS800, more specimens failed at the higher-strength regime than at the lower-strength regime, resulting in a bi- or tri-modal strength distribution.

An average value of post-impact strength at each (high and low) strength regime was utilized to better represent the post-impact strength behavior of both silicon nitrides, and the results are shown in Figure 4. This figure clearly shows features such as the two strength regimes, the strength envelope between the related impact velocities, and the critical impact velocity, etc. From these results as well as from Figure 2, it can be concluded that resistance to FOD is greater in AS800 than in SN282, consistent with the previous FOD results on flexure bar specimens at ambient temperature [11,12].

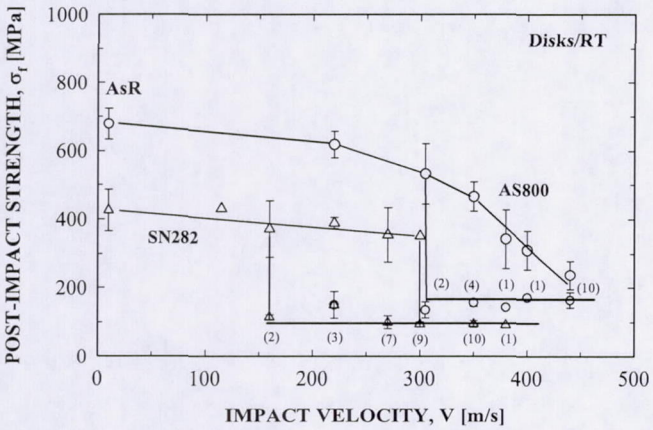

Figure 4. Mean post-impact biaxial strength as a function of impact velocity for AS800 and SN282 silicon nitrides disks impacted by 1.59-mm-diameter steel ball projectiles. Error bars indicate ±1.0 standard deviation. "AsR" indicates as-received biaxial flexure strength of each material. The numbers in the parentheses represent the number of test specimens failed at the lower strength regime.

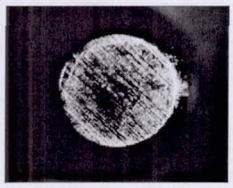

Figure 5. A typical example of a flattened steel ball projectile subjected to an impact velocity of 220 m/s to AS800 silicon nitride.

Impact Morphology and Fractographic Analysis

Steel-ball projectiles

Some of the steel-ball projectiles were collected upon impact for fractographic analysis. The hardened steel-ball projectiles were flattened after impact as a result of accompanying plastic deformation. In some cases, the projectiles were subjected to both extreme heat evidenced by burning marks and cracking, particularly at higher impact velocity. The degree of plastic deformation of the projectiles in terms of projectile-diameter decrease was about 20 to 40 % depending on impact velocity. Also note that the flattened surfaces of the steel-ball projectiles retained the impression of the machining marks of ceramic target specimens with a series of numerous parallel lines, indicative of a significant severity of impact involved, as shown in Figure 5.

Contact areas/impressions

The tensile principal stress, according to the Hertzian contact analysis, occurs just outside the contact area between two contacting bodies in which a cone crack initiates and propagates through the locus of maximum tensile stress [5,9]. In cases of impacts with hard projectiles vs. hard target materials (such as ceramic balls vs. ceramic target materials), it has been shown that agreement between the calculated contact area (radius) and the upper size (radius) of a cone was reasonable [4]. The contact area can be estimated based on the Hertzian contact theory together with the principle of conservation of impact energy as follows [1,4,5,8]:

$$a = \alpha (k/E)^{1/5} \rho^{1/5} R\, V^{2/5} \tag{2}$$

where a is the radius of contact area, α is a constant (≈1.3), E is the elastic modulus of the target material, ρ is the density of the projectile, R is the radius of the projectile, and V is the impact velocity. The parameter k is expressed as

$$k = (1-\nu^2) + (1-\nu'^2)\frac{E}{E'} \tag{3}$$

where ν is Poisson's ratio and the primes denote variables associated with the projectile. The calculated contact area based on Eq. (2) was significantly (almost twice) greater than the impression sizes observed. However, it should be noted that a direct comparison should not be made between the calculated and the observed since the calculated contact size was unrealistically large, which were well in the range of plastic deformation of the impacting projectiles. As a consequence, the impact events in this work can be characterized as 'plastic (in projectile)-elastic (in target material)' rather than 'elastic-elastic' impact that is the case for ceramic balls vs. ceramic target. It is interesting to note that a consistent size (0.23-mm diameter) of upper cones was observed regardless of impact velocity. This is contradictory to the Hertzian contact theory, which states that the contact area increases with increasing impact velocity and that the tensile principal stress occurs just outside the contact area between two contacting bodies in which a cone crack initiates and propagated through the locus of maximum tensile stress [5,9]. The discrepancy is again believed to be a result of significant plastic deformation in which Hertzian contact theory might not be applicable.

Fracture surfaces/modes

At lower impact velocities, failure from ring cracks was common to both AS800 and SN282 specimens. Part of the ring contour was seen at the failure origin as a small curved portion, as shown in Figure 6(a). The fracture surfaces also portrayed such a curved portion.

At intermediate impact velocities for each material, both ring and radial cracks were associated with failure. The upper cones located at the impact center, whether somewhat well developed or not, seemed to be rarely associated as failure origins. The failure location of ring cracks, measured from the impact center, was 0.28±0.07 mm (or 0.56-mm diameter). This indicates that the strength-controlling ring cracks were situated between the (inner) impression diameter (=0.82 mm) and the upper cone diameter (=0.23 mm). The lower-strength regime, typified at intermediate impact velocities of each material, was associated exclusively with well-developed radial cracks ranging in size from 3 to 5 mm, emanating from the impact sites, as shown in Figure 6(b). These well-developed radial cracks resulted in the lower-regime strength of about 150 and 100 MPa, respectively, for AS800 and SN282. Hence, it is important to note that the existence of lower strength regime was due to the occurrence of these significant radial cracks.

At higher impact velocities close to or above the critical impact velocity, failure of both materials was mainly associated with well-eveloped radial cracks although well-developed cone cracking occurred simultaneously and invariably. In many cases, cones with lower

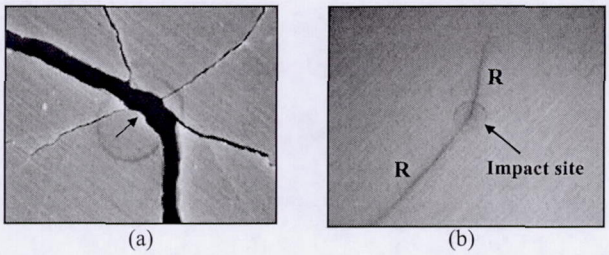

(a) (b)

Figure 6. Typical examples of impact damage of AS800 target specimens at lower impact velocity: (a) fracture origin (arrowed) emanating from a ring crack (V=220 m/s; strength=616 MPa); (b) radial cracks (designated with 'R') emanating from impact site (V=220 m/s; strength=151 MPa, controlled by the lower radial crack with a size of 4.7 mm).

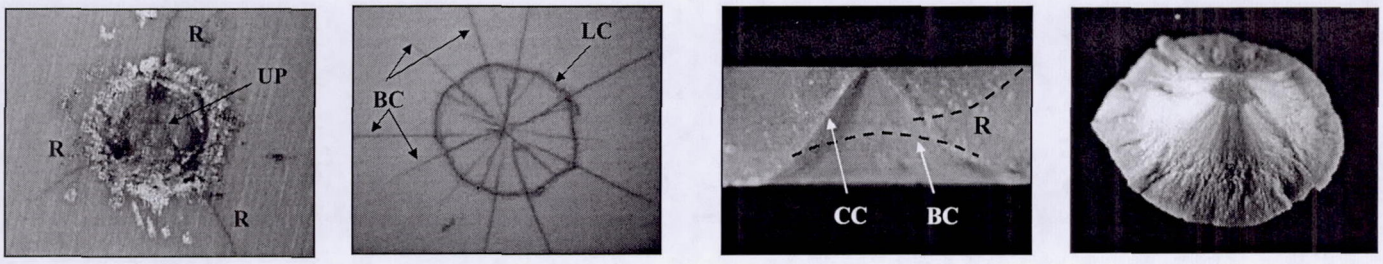

(a) (b) (c) (d)

Figure 7. Typical examples of impact damages of an AS800 silicon nitride disk impacted at a high velocity of 440 m/s by a 1.59-mm-diameter steel ball projectile: (a) impact site showing impression, radial cracks (R), and upper cone (UP) before strength testing; (b) backside view showing backside radial cracks (BC, radiating from the center) and lower diameter of a cone (LC) before strength testing; (c) fracture surface showing a cavity of a cone (CC), impact-site radial cracks (R), and backside radial cracks (BC); (d) a separated cone with a lower diameter of about 5 mm.. Strength= 192 MPa.

diameters ranging from 4 to 6 mm were separated from the specimens after strength testing. Typical examples showing impression, radial cracks, upper cone, backside cracks (this will be discussed later), fracture surface, and a separated cone are shown in Figure 7. The geometry of cones, including upper and lower cone diameters and heights of cones, was determined for both silicon nitrides from either fracture surfaces or separated cones using typically 7 specimens available in measurements at each high impact velocity. The cone angle, defined as half of apex angle, was calculated based on the determined cone geometry.* The cone angle, with an average value of 42 ± 2°, remained almost unchanged regardless of material over impact velocities from 350 and 440 m/s. Limited information on cone angle for the case of impact of ceramic target by steel ball projectiles exists in the literature with only a form of photographs (e.g., [20]), so a meaningful comparison between this work and the published data could not be made. However, it should be noted that the angle also depends on variables such as specimen geometry, type of specimen support, projectile material, and impact velocity, etc.

In the simultaneous presence of ring, radial, and cone cracks, the radial cracks were most influential in controlling the magnitude of post-impact strength. The probability of radial cracking for a given impact velocity was greater in SN282 than in AS800, attributed to lower fracture toughness of SN282. Radial cracking initiated with a low probability (10-20 %) at 160 and 220 m/s for SN282 and AS800, respectively. The critical impact velocity of 300 and 440 m/s for SN282 and AS800, respectively, corresponded to the situation at which radial cracking occurred with a 100 % probability for both silicon nitrides. Although not presented here, a prediction of strength as a function of radial crack size was made based on a semi-circular crack assumption and was found in good agreement with the experimental data [21]. This implies that the necessity of detailed knowledge on complex radial crack geometry/configuration (such as non-symmetrical and significant elliptical shapes) involved in radial cracking would be minimized or eliminated. A routine measurement of (maximum) radial surface cracks and the use of a simple semi-circular assumption could give a reasonable estimation of prospective post-impact or potential component strength.

* Strictly speaking, the cones were not straight but a little curved particularly toward their bottom. The calculation of cone angle, however, was made based on the straight line extended to the bottom in some cases.

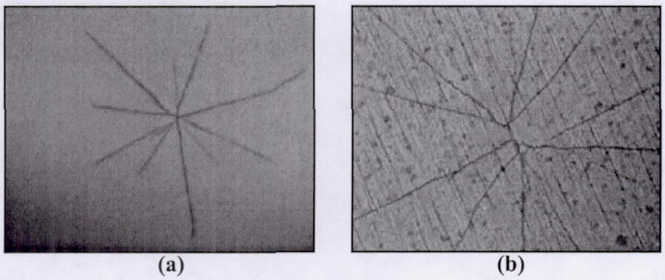

(a) (b)

Figure 8. Typical examples of well-developed backside radial cracking: (a) AS800 silicon nitride disk impacted at 300 m/s (before strength testing); (b) SN282 silicon nitride disk impacted at 300 m/s (before strength testing). The corresponding post-impact strength was 450 and 96 MPa, respectively, for the AS800 and SN282 specimens. Significant crack sizes ranged from 4 to 7 mm.

Backside cracking and its analytical consideration

Unlike flexure bar specimens, disk target specimens exhibited a peculiar feature of backside cracking that occurred on the reverse side of disks depending on impact velocity. Typical backside cracking generated upon impact -but prior to post-impact strength testing- is shown in Figure 8. Well-defined radial cracks originated in the reverse side of the specimen from a point just beneath the impact site. The crack configuration was semi-elliptical with minor to major axis ratio of about 0.2-0.3. Backside cracking initiated with a low probability of 20-30% at 160 and 220 m/s for SN282 and AS800, respectively, and it reached 100 % probability at velocity of $V \geq 350$ m/s for both silicon nitrides. The sizes of backside cracks, measured from its center, were almost constant for AS800 independent of impact velocity with a mean size of about 6 mm; whereas, SN282 showed a dependency of crack size on impact velocity such that crack size increased from 4 to 7 mm with increasing impact velocity.

The reason for the occurrence of backside cracking has been considered using an *elastic foundation* approach [21]. Although the target specimens were rigidly supported, due to the significant impact force (estimated conservatively by the quasi-static contact theory [1,4,5,8]), it was postulated that they might respond as though supported on an elastic foundation. Any deflection of the elastic foundation would result in bending of the target specimens, which in turn would induce a tensile stress field on the reverse of the specimen. The results of maximum tensile stress estimated using the elastic foundation approach [22] are shown in Figure 9, where the maximum tensile stress was plotted as a function of impact force for three different beam widths (b) and two different types of elastic supports. For b=10 mm, relatively smaller than the target specimen's diameter, the maximum tensile stress at P=25 kN corresponding to the case (V=350 m/s) where all of the AS800 and SN282 disks exhibited backside cracking, was 240 and 270 MPa, respectively, for silicon nitride and steel supports. For b=30mm, which might provide a better representation of the actual target specimen diameter, the respective maximum tensile stress was 80 and 90 MPa. Hence, the estimated maximum tensile stress based on the elastic foundation approach was much lower than the target material's strength and consequently insufficient to cause backside cracking. Although several simplifying assumptions were used in the estimation and their justification must be verified, the elastic foundation approach gives an insight into the reason for the occurrence of backside cracking at least qualitatively. If the target specimens with backside cracks were regarded as actual structural components under service with unexpected, varying load conditions, the strength/reliability of the components, as a consequence, should be based on a degree of severity of backside cracking: For example, the strength of disks containing backside cracks with an average size of 6 mm, called *backside strength*, was only 130 and 90 MPa, respectively, for AS800 and SN282. Because of the occurrence of backside cracking, the lower and upper limits of impact velocities have to be reconstructed for a structural design point of view. The backside cracking was also observed recently for intermetallic disks [23] as well as for silicon nitride disks [24].

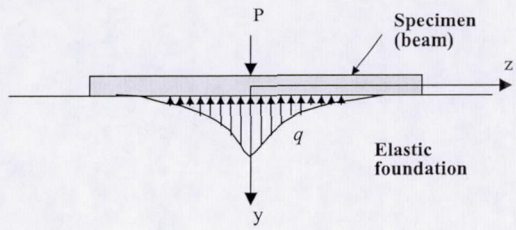

(a)

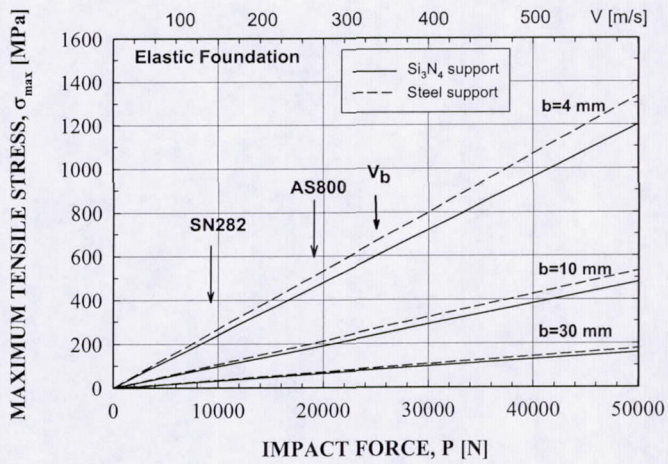

(b)

Figure 9. (a) Specimen/elastic-foundation subjected to a concentrated load (impact); (b) Maximum tensile stress as a function of impact force occurring on the reverse side of a disk at a point opposite to impact site [21,22]. Impact force was estimated by the idealized quasi-static contact theory [1,4,5,8]. The initiation velocity for backside cracking is indicated as an arrow for each material. V_b is a velocity (=350 m/s) that resulted in 100 % backside cracking for both AS800 and SN282 silicon nitrides.

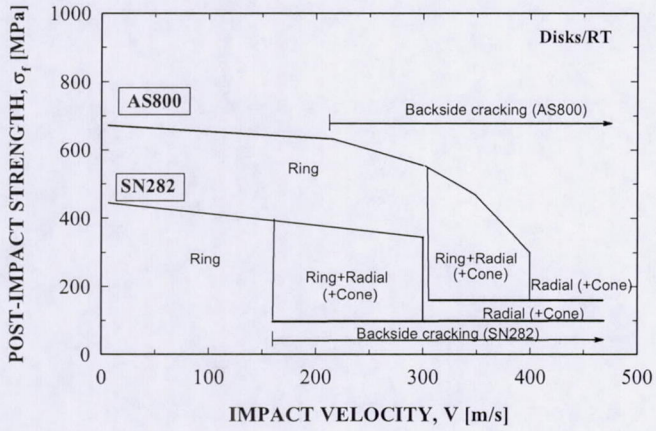

Figure 10. Fracture map constructed for AS800 and SN282 silicon nitride disks impacted by 1.59-mm-diameter steel ball projectiles at ambient temperature. The range of impact velocity for backside cracking is also included. "(+Cone)" represents cone cracking but not associated with strength controlling flaws.

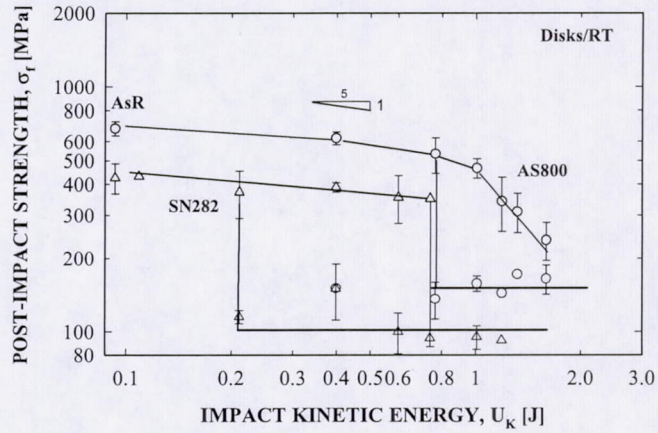

Figure 11. Post-impact strength as a function of impact kinetic energy for AS800 and SN282 silicon nitrides disks impacted by 1.59-mm-diameter steel ball projectiles. The slope of 1/5 indicates a theoretical value based on Eq. (5). The error bars indicate ±1.0 standard deviations. "AsR" indicates as-received biaxial flexure strength of each material.

Fracture map (summarized)

As aforementioned, several different types of damage/cracking including ring, radial, cone, and backside cracks were individually or simultaneously generated in disk target specimens, depending on impact velocity. Figure 10 shows a fracture map, which summarizes the types of damages/cracks with respect to impact velocity for both AS800 and SN282 silicon nitrides based on the results of impact morphologies and fractographic analysis. At low impact velocities for each material, ring cracks were dominant and controlled the post-impact strength. At intermediate velocities, ring and radial or cone (a rare case) cracks were prevailing, and the ring or radial cracks determined the post-impact strength; radial cracking increased with increasing impact velocity. At or above the critical impact velocities, both well-developed radial and cone cracks occurred; however, the radial cracks uniquely controlled the post-impact strength.

Figure 10 also includes the range of impact velocities where backside radial cracking for each silicon nitride takes place. Cone cracking started to develop at intermediate velocities, and was very well developed at or above the critical impact velocity. Although cone cracks would not affect component strength significantly in view of their geometry and size compared with the severity of radial cracks, they are responsible for material loss when the cones are formed through the thickness of a component and then separated from the component. This problem would be significant if one of the requirements of the component is of some type of sealing, separation, and/or environmental barriers.

Analytical Considerations of Strength Degradation

A phenomenological model of strength degradation due to *ball impact* was proposed previously by Wiederhorn and Lawn [1], based on assumptions that the impact event was elastic and quasi-static and that strength degradation was attributed to a formation of cone cracks. Also, another important assumption was that the "effective" size of strength controlling flaws was proportional to the base radius of the cone [1,5,9]. The latter simplification was based on the fact that the stress intensity factor solution of a cone crack was not available and that the geometry of a cone crack system varied with projectile, target materials and impact conditions (velocity), etc. With those assumptions, strength degradation was modeled using Hertzian contact analysis, the principle of energy conservation, and indentation fracture relations. The model, despite several assumptions, was in good agreement with experimental data determined for glass impacted by steel or tungsten carbide spherical projectiles [1]. The resulting strength degradation as a function of impact velocity is expressed as follows [1]:

$$\sigma_f = \Phi (k/E)^{2/15} \rho^{-1/5} R^{-2/3} K_{IC}^{4/3} V^{-2/5} \tag{4}$$

where Φ is a constant and K_{IC} is fracture toughness of target material. Equation (4) can also be expressed in terms of impact kinetic energy, $U_K = mV^2/2$ with m being the projectile mass, to yield

$$\sigma_f = \Phi' (k/E)^{2/15} R^{-1/15} K_{IC}^{4/3} U_K^{-1/5} \tag{5}$$

where $\Phi' = (2\pi/3)^{1/5} \Phi$. For a given target material and a given material and geometry of a projectile, the post-impact strength depends on [impact velocity]$^{-2/5}$ or [impact kinetic energy]$^{-1/5}$ as seen from Eq. (4) or (5).

The post-impact strength (log σ_f) data shown in Figure 4 were plotted as a function of impact kinetic energy (log U_K) in Figure 11 based on Eq. (5). It is noted from the figure that the discrepancy in slope between the prediction (=-1/5) and the experimental data seemed insignificant at impact energy of U_K<0.8 J (V<300 m/s) for both AS800 and SN282, except for the lower-strength regime of SN282. However, the discrepancy was significant above U_K>0.8 J for AS800 at the upper strength regime while SN282 is already at the lower-strength regime,

i.e., $V \geq V_c$. The strength degradation model (Eq. 4 or 5) assumed that cone cracks are the dominant strength controlling flaws. However, as seen in this work (e.g., see the fracture map in Figure 10), cone cracking rarely controlled post-impact strength; instead ring or radial cracks did control the strength in most cases. In addition, several different types of flaws were associated individually or simultaneously in the impact event, depending on impact velocity. Hence, the cone-cracking model, Eq. (4 or 5), would not be appropriate to describe adequately the post-impact biaxial strength behavior of AS800 and SN282 silicon nitrides, as also observed previously from uniaxial flexure beam target specimens [11,12]. One of the reasons for this is that the significant plastic deformation of a projectile upon impactdeviates remarkably from the model's assumption of idealized elastic impact. The complex nature of cracking behavior and the considerable plastic deformation of projectiles encountered in this work would be the most hindering factors to develop a unified strength degradation model applicable over a wide range of impact velocities. This again gives one a precaution that a routine use of any program/software would never be made without thorough understanding of failure/deformation mechanisms involved. Furthermore, because of the inherent scatter of post-impact strength caused by the different types of damage/cracking generated, use of only a few specimens at a given impact velocity might result in a serious misinterpretation on overall impact behavior,and hence, should be avoided.

Key Material Parameter to FOD Resistance

Although the model (Eq. 4 or 5) does not predict the post-impact strength behavior in a wide range of impact energy, it has shown to be able to determine a key material parameter to affect the resistance to FOD [11,12]. For most silicon nitrides, elastic modulus (E), hardness, density, and Poisson's ratio (ν) are quite similar. For a given projectile, impact velocity, and given target specimen geometry, the post-impact strength, according to Eq. (4 or 5), depends on the fracture toughness of a target material with a relation of $\sigma_f \propto [K_{IC}]^{4/3}$. This leads to a simple expression of the post-impact strength ratio between AS800 and SN282 silicon nitrides as follows

$$\frac{\sigma_{f/AS800}}{\sigma_{f/SN282}} = [\frac{K_{IC/AS800}}{K_{IC/SN282}}]^{4/3} \qquad (6)$$

Use of this relation together with the values of fracture toughness (see Table 1) determined for both AS800 and SN282 yielded that the post-impact strength of AS800 was 1.68 times greater than that of SN282. The actual strength ratio at 220 m/s and 300 m/s (only available velocities for comparison) was found to be 1.6 and 1.5, respectively, resulting in good agreement. It would be reasonable to conclude that a silicon nitride with greater fracture toughness can possess greater FOD resistance than another silicon nitride with lower fracture toughness, as also seen in the previous study with flexure bar specimens [11,12]. In the previous study [11,12], the major issue on the key material parameter (K_{IC}) has been investigated more extensively using an additional conventional, equiaxed, fine-grained silicon nitride (NC132), as summarized in Figure 12 as critical impact velocity as a function of fracture toughness [12]. The general trend manifest from the figure is that critical impact velocity increases with increasing fracture toughness, leading to the conclusion that fracture toughness is a key material parameter affecting FOD resistance in silicon nitrides. This is also understandable if one considers that fracture toughness is a measure of resistance to crack initiation and propagation.

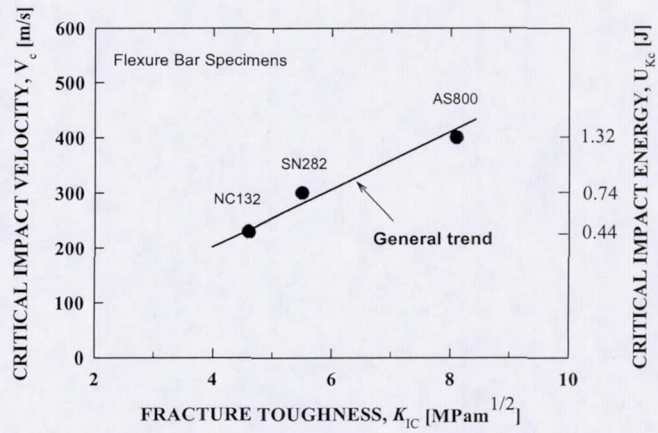

Figure 12. General trend of critical impact velocity as a function of fracture toughness for two *in-situ* toughened AS800 and SN282 silicon nitrides and one equixed fine-grained NC132 silicon nitride [12].

Comparisons

Projectiles: 'blunt' vs. 'sharp'

A comparison of post-impact biaxial strength of silicon nitrides between "blunt" steel-ball impact (this study) and "sharp" SiC-particles (grit # 16 and 46) impact [3,25] is shown in Figure 13. Note a considerable strength degradation for the case of sharp particle impact occurring even at much lower impact kinetic energy, showing that the severity of impact damage was far greater in "sharp" particle impact than in "blunt" (steel-ball) projectile impact. The sharp, more elastic particle impact by SiC particles typically produced radial cracks emanating from the impact sites (similar to the Vickers indent cracks that originate from the corners of an impression site), thereby resulting in significant strength degradation. It should be noted that fracture toughness of AS440 silicon nitride was greater (about 30%) than that of GN10 silicon nitride; hence, as expected, post-impact strength in sharp particle impact was greater for AS440 than for GN10. The results in Figure 13 show again that for a given target material and a given impact energy, the geometry and material of projectiles are very important parameters affecting post-impact strength or FOD behavior of advanced ceramics.

Target specimens: disks vs. flexure bars

Figure 14 shows a comparison of post-impact strength behavior between the biaxial disks (2-mm thickness and 45-mm diameter) in this work and the uniaxial flexure bars (4 mm x 3 mm x 45 mm in width, depth and length, respectively) in the previous work [11,12]. Both disks and flexure bars were rigidly supported and the same steel-ball projectiles were used. For a given impact velocity, the overall post-impact strength was higher for uniaxial flexure bars than for biaxial disks because of the size effect.[#]

[#] A prediction of strength from one specimen configuration (uniaxial) to another (biaxial) was made using the principle of independent action (PIA, Weibull statistics) with surface flaws for as-received specimens. The ratio of predicted biaxial to uniaxial strength (as-received) was 0.90 and 0.82 for AS800 and SN282, respectively; whereas, the ratio of actual biaxial and uniaxial strength

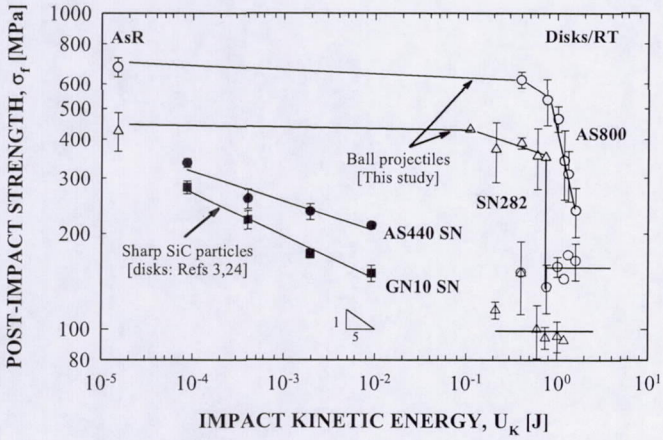

Figure 13. Comparison of post-impact biaxial strength as a function of impact kinetic energy between "sharp" SiC particle impact for AS440 and GN10 silicon nitrides [3,24] and "blunt" steel ball projectile impact (this work). The error bars indicate ±1.0 standard deviations. A theoretical slope (=1/5) is included.

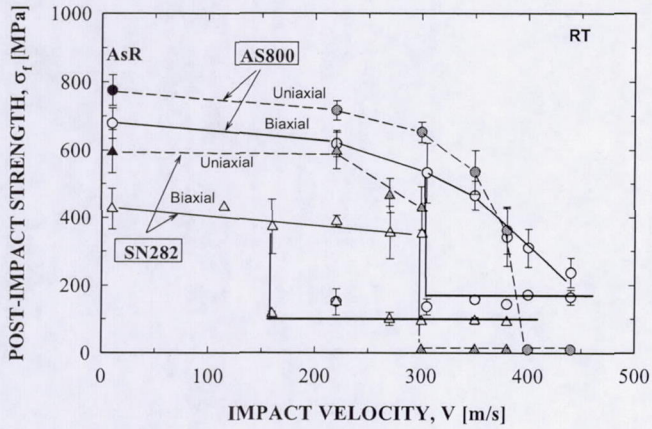

Figure 14. Comparison of post-impact strength as a function of impact velocity between uniaxial flexure bars [11,12] and biaxial disks [this study] of AS800 and SN282 silicon nitrides impacted by 1.59-mm-diameter steel ball projectiles at ambient temperature. "AsR" indicates as-received uniaxial and biaxial flexure strength of both materials. The error bars indicate ±1.0 standard deviations.

The critical impact velocity for uniaxial bars was $V_c \approx 300$ and 400 m/s for SN282 and AS800, respectively, while for biaxial disks it was $V_c \approx 300$ m/s and 440 m/s for SN282 and AS800, respectively, resulting in basically good agreement in V_c between the two different specimen configurations. However, the lower-strength regime uniquely occurring in biaxial disks was not seen in uniaxial flexure bars, primarily due to the difference in specimen thickness - thin (disks) versus thick (flexure bars). Furthermore, the backside cracking characterized in biaxial disks did not exhibit in flexure bars, possibly again due to the difference in specimen thickness, as noted by the *elastic-foundation* approach. Although the general trend of post-impact strength with respect to impact velocity seemed similar in both specimen configurations, the occurrence of significant radial and backside cracking was very different from one specimen configuration to another. This implies that a particular set of impact data generated under particular impact conditions may not be universally applicable to a wide range of applications.

Other Factors of Consideration

Designing aeroengine components to withstand FOD events is a complex task. Consideration of many factors is required, both in the generation of FOD data as well as in actual component design efforts. A sample of these numerous factors includes the following:

- Effect of projectile material/geometry
- Effect of test specimen material/geometry
- Effect of test-specimen support and component attachment
- Effect of temperature/environment
- Appropriate protective coatings
- Geometrical component design to enhance FOD resistance
- FOD/Reliability/Life prediction methodologies

Not only must each of these factors be scrutinized individually, but the effects of interactions between multiple factors also must be accommodated. Notwithstanding the immense challenges this poses, a strategy for mitigating FOD damage must be developed and employed in order to achieve the most desirable performance of components in service. Hence, some of these factors are immediate subjects of study and the related work is under way, such as in the tasks reported in this manuscript. Others are long-term efforts and are pursued continually in the quest for improving the efficiency and reliability of aeroengine components.

CONCLUSIONS

Based on the results of FOD testing using biaxial disks at ambient temperature for two in-situ toughened, gas-turbine grade silicon nitrides (AS800 and SN282), following conclusions were made:

1) The overall resistance - estimated by post-impact strength - to foreign object damage (FOD) by 1.59-mm-diameter steel-ball projectiles was found to be greater for AS800 silicon nitride than for SN282 silicon nitride in an impact velocity range from 115 to 440 m/s, due to greater fracture toughness of AS800.
2) The critical impact velocity, in which biaxial disk target specimens exhibited the lowest post-impact strength, was about 440 m/s and 300 m/s, respectively, for AS800 and SN282 silicon nitrides. The occurrence of critical impact velocity was associated with the generation of significant sizes (4-7 mm) of radial cracks originating from the impact sites.
3) No single crack system was involved in impact event with increasing impact velocity, resulting in several different types of flaws associated individually or simultaneously. A fracture map was proposed to identify the occurrence of particular crack

---

was found to be 0.89 and 0.72. From excellent to reasonable agreement was found for AS800 and SN282 specimens, respectively. Weibull modulus was taken in this prediction as m=20 and 10 for AS800 and SN282, respectively.

systems including ring, radial, cone, and backside cracking with respect to impact velocity.

4) In terms of the difference of specimen geometry/configuration, the degree of additional damage by radial and backside cracking was much more severe in thin biaxial specimens than in thick uniaxial flexure bars. This indicates that a particular set of impact data generated under particular impact conditions may not be universally applicable to a variety of applications. A case-by-case approach to specific geometry/configuration should be taken into consideration.
5) It should be noted that the test specimen configuration used in this work may not be representative of actual engine components. Hence, future work should include the effect of specimen supports on FOD to relate to engine components such as blades and vanes.

Acknowledgements

The authors are thankful to R. Pawlik for the experimental work during the course of this study. This work was supported by Higher Operating Temperature Propulsion Components (HOTPC) program, NASA Glenn Research Center, Cleveland, Ohio.

REFERENCES

1. S. M. Wiederhorn and B. R. Lawn, "Strength Degradation of Glass Resulting from Impact with Spheres," *J. Am. Ceram. Soc.*, **60**[9-10] 451-458 (1977).
2. S. M. Wiederhorn and B. R. Lawn, "Strength Degradation of Glass Impact with Sharp Particles: I, Annealed Surfaces," *J. Am. Ceram. Soc.*, **62**[1-2] 66-70 (1979).
3. J. E. Ritter, S. R. Choi, K. Jakus, P. J. Whalen, and R. G. Rateick, "Effect of Microstructure on the Erosion and Impact Damage of Sintered Silicon Nitride," *J. Mater. Sci.*, **26** 5543-5546 (1991).
4. Y. Akimune, Y. Katano, and K. Matoba, "Spherical-Impact Damage and Strength Degradation in Silicon Nitrides for Automobile Turbocharger Rotors," *J. Am. Ceram. Soc.*, **72**[8] 1422-1428 (1989).
5. C. G. Knight, M. V. Swain, and M. M. Chaudhri, "Impact of Small Steel Spheres on Glass Surfaces," *J. Mater. Sci.,* **12** 1573-1586 (1977).
6. A. M. Rajendran and J. L. Kroupa, "Impact Design Model for Ceramic Materials," *J. Appl. Phys*, **66**[8] 3560-3565 (1989).
7. L. N. Taylor, E. P. Chen, and J. S. Kuszmaul, "Microcrack-Induced Damage Accumulation in Brittle Rock under Dynamic Loading," *Comp. Meth. Appl. Mech. Eng.*, **55**, 301-320 (1986).
8. R. Mouginot and D. Maugis, "Fracture Indentation beneath Flat and Spherical Punches," *J. Mater. Sci.*, **20** 4354-4376 (1985).
9. A. G. Evans and T. R. Wilshaw, "Dynamic Solid Particle Damage in Brittle Materials: An Appraisal," *J. Mater. Sci.*, **12** 97-116 (1977).
10. B. M. Liaw, A. S. Kobayashi, and A. G. Emery, "Theoretical Model of Impact Damage in Structural Ceramics," *J. Am. Ceram. Soc.*, **67** 544-548 (1984).
11. S. R. Choi, J. M. Pereira, L. A. Janosik, and R. T. Bhatt, "Foreign Object Damage of Two Gas-Turbine Grade Silicon Nitrides at Ambient Temperature," *Ceram. Eng. Sci. Proc.*, **23**[3] 193-202 (2002).
12. S. R. Choi, J. M. Pereira, L. A. Janosik, and R. T. Bhatt, "Foreign Object Damage Behavior of Two Gas-Turbine Grade Silicon Nitrides by Steel Ball Projectiles at Ambient Temperature," NASA/TM-2002-211821, National Aeronautics & Space Administration, Glenn Research Center, Cleveland, OH (2002).
13. S. R. Choi and J. P. Gyekenyesi, (a) "Elevated-Temperature "Ultra"-Fast Fracture Strength of Advanced Ceramics: An Approach to Elevated-Temperature "Inert" Strength," *ASME J. Eng. Gas Turbines & Powers*, **121** 18-24 (1999); (b) "'Ultra'-Fast Strength of Advanced Structural Ceramics at Elevated Temperatures" pp. 27-46 in *Fracture Mechanics of Ceramics*, Vol 13, Edited by R. C. Bradt, D. Munz, M. Sakai, V. Ya. Shevchenko, and K. W. White, Kluwer Academic/Plenum Publishers, New York, NY (2002).
14. S. R. Choi and J. P. Gyekenyesi, "Slow Crack Growth Analysis of Advanced Structural Ceramics under Combined Loading Conditions: Damage Assessment in Life Prediction Testing," *ASME J. Eng. Gas Turbines & Power*, **123** 277-287 (2001).
15. ASTM C 1259, "Test Method for Dynamic Young's Modulus, Shear Modulus, and Poisson's Ratio for Advanced Ceramics by Impulse Excitation of Vibration," *Annual Book of ASTM Standards*, *Vol. 15.01*, ASTM, West Conshohocken, PA (2002).
16. ASTM C 1327, "Test Method for Vickers Indentation Hardness of Advanced Ceramics," *Annual Book of ASTM Standards*, *Vol. 15.01*, ASTM, West Conshohocken, PA (2002).
17. ASTM C 1161, "Test Method for Flexural Strength of Advanced Ceramics at Ambient Temperatures," *Annual Book of ASTM Standards*, *Vol. 15.01*, ASTM, West Conshohocken, PA (2002).
18. ASTM C 1421, "Test Methods for Determination of Fracture Toughness of Advanced Ceramics at Ambient Temperature," *Annual Book of ASTM Standards*, *Vol. 15.01,* ASTM, West Conshohocken, PA (2001).
19. D. K. Shetty, A. T. Rosenfield, P. McGuire, G. K. Bansal, and W. H. Duckworth, "Biaxial Flexure Test for Ceramics," *Ceram. Bull.,* **59**[12] 1193-1197 (1980).
20. Y. Akimune, T. Akiba, and T. Ogasawara, "Damage Behavior of Silicon Nitride for Automotive Gas Turbine Use When Impacted by Several Types of Spherical Particles," *J. Mater. Sci.*, **30** 1000-1004 (1995)
21. S. R. Choi, J. M. Pereira, L. A. Janosik, and R. T. Bhatt, "Foreign Object Damage in Disks of Two Gas-Turbine Grade Silicon Nitrides by Steel Ball Projectiles at Ambient Temperature," prepared for a NASA/TM, National Aeronautics & Space Administration, Glenn Research Center, Cleveland, OH.
22. A. P. Boresi, O. M. Sidebottom, F. B. Seely, and J. O. Smith, Advanced Mechanics of Materials (3rd Edition), pp.369-377, John Wiley & Sons, NY (1978); also see any text books related.
23. M. V. Nathal and S. L. Draper, "Ballistic Impact Response of Advanced Silicide Alloys in the IHPTET Program - Preliminary Report," National Aeronautics & Space Administration, Glenn Research Center, Cleveland, OH (2002).
24. Y. Hara, K. Matsubara, K. Mizuno, T. Shimamori, and H. Yoshida, "Development and Evaluation of Silicon Nitride Components for Ceramic Gas Turbine," ASME paper 98-GT-498.
25. S. R. Choi, J. E. Ritter and K. Jakus, "Erosion and Impact Behavior of Various Advanced Ceramics at Ambient and Elevated Temperatures," unpublished work, University of Massachusetts, Amherst, MA (1988).